Available online at www.sciencedirect.com

ScienceDirect

Ceramics International 40 (2014) 651–657

CERAMICS INTERNATIONAL

www.elsevier.com/locate/ceramint

Synthesis and characterization of $Nd_2Sn_xZr_{2-x}O_7$ pyrochlore ceramics

Linggen Kong*, Yingjie Zhang, Inna Karatchevtseva, Mark G. Blackford, Gregory R. Lumpkin, Gerry Triani

Institute of Materials Engineering, Australian Nuclear Science and Technology Organization, Locked Bag 2001, Kirrawee DC NSW 2232, Australia

Received 2 May 2013; received in revised form 7 June 2013; accepted 14 June 2013
Available online 21 June 2013

Abstract

Pyrochlore structured $Nd_2Sn_xZr_{2-x}O_7$ ($x=0$–2) ceramics were prepared by a new chemical synthesis route in an aqueous media. Raman spectra and X-ray diffraction patterns confirmed the formation of the pyrochlore structure after sintering at 1400 °C. SEM results showed pelletized materials became dense with increasing Zr/Sn mole ratio and sintering temperature. These candidate materials have characteristic structures for the development of nuclear waste forms or inert matrix nuclear fuels.

Keywords: Pyrochlore; Neodymium zirconate; Neodymium stannate; Chemical synthesis.

1. Introduction

For applications in nuclear waste forms and inert matrix nuclear fuels, dense and radiation tolerant ceramics are essential to ensure these materials are capable of maintaining adequate strength under extreme environments experienced during service, *e.g.*, elevated temperature, high radiation fields, and chemical attack. Mixed oxide compositions utilizing SnO_2 have been reported to be difficult to obtain high density materials because of the predominance of non-densifying mechanisms for mass transport such as evaporation/condensation (above 1300 °C) and surface diffusion (below 1100 °C). These mechanisms are responsible for grain growth and neck formation between particles during sintering but do not promote densification [1–6]. Consequently, ceramics utilizing SnO_2 in its composition have porosities up to 40%, which may be appropriate for gas sensing applications, but undesirable in applications requiring mechanical strength [6]. Even when very fine SnO_2 powder coupled with high pressure processing ceramics prepared from multi-component mixed oxide formulations improve their sinterability, it is desirable to use mixing precursors in molecular level for easier densification as opposed to a mixture of oxide nanoparticles as each one has its own sintering behavior, thus enhancing the risk of resulting heterogeneity.

As nuclear waste forms, structures based on titanate, zirconate and stannate pyrochlores have been investigated extensively [7–16]. In contrast to lanthanide titanate pyrochlores ($Ln_2Ti_2O_7$) which are generally susceptible to radiation-induced amorphization, the lanthanide stannate pyrochlores ($Ln_2Sn_2O_7$) show a much greater variability in their response to ion irradiation [7]. However, one of the contributing factors to this variability has been the difficulty in forming of dense lanthanide stannate pyrochlore ceramics. Alternatively, pyrochlore lanthanide zirconate ceramics ($Ln_2Zr_2O_7$) possess desirable physico-chemical properties such as high thermal stability, high phase stability, high chemical resistance and durability [8–12]. In addition, lanthanide zirconates also have remarkable resistance to amorphization under ion beam irradiation [7–16].

The purpose of this study is to synthesize and characterize pyrochlore structured ceramics by gradually replacing Sn with Zr in the composition and to investigate the sintering behavior

*Corresponding author. Tel.: +61 2 9717 3630; fax: +61 2 9717 9225.
E-mail address: lnk@ansto.gov.au (L. Kong).

0272-8842/$ - see front matter © 2013 Elsevier Ltd and Techna Group S.r.l. All rights reserved.
http://dx.doi.org/10.1016/j.ceramint.2013.06.051

of powders and compacts while maintaining the pyrochlore structure. A series of neodymium stannate zirconate $Ln_2Sn_xZr_{2-x}O_7$ ceramics (x=0, 0.5, 1, 1.5, and 2) were prepared by the co-precipitation method in aqueous media. Contrary to traditional zirconium alkoxides which are sensitive to moisture, in this study Tyzor ZEC was employed as Zr precursor which is insensitive to water, thereby allowing the processing to be conducted in an aqueous phase. The formation of the pyrochlore super-structure in $Ln_2Sn_xZr_{2-x}O_7$ powder was monitored including the density and the porosity of the compacts as a function of sintering temperature following the substitution of Zr for Sn.

2. Material and methods

Neodymium(III) nitrate hexahydrate (99.9%+), zirconium (IV) bis(diethyl citrato)dipropoxide or Tyzor® ZEC containing 12 wt% ethanol and 12 wt% 1-propanol (product of DuPont™), tin(IV) chloride pentahydrate (98%+), and oxalic acid (98%+) were purchased from Aldrich and used as received. The zirconium content in Tyzor ZEC was determined by gravimetric analysis. All chemicals were A.R. grade, with Milli-Q grade water being used in all experimental procedures.

In the preparation of precipitates with specific compositions of NdSn and NdZr, the following procedures were adopted. For the synthesis of NdSn precipitate, 60 mmol of oxalic acid was used to precipitate 15 mmol neodymium nitrate and 15 mmol tin(IV) chloride in aqueous phase at pH=7.0–7.2 by addition of 1.667 M ammonia aqueous solution. For the synthesis of NdZr precipitate, 15 mmol Tyzor ZEC was complexed with 15 mmol neodymium nitrate at pH=8.0–8.3 by addition of 1.667 M ammonia aqueous solution. The above precipitates were centrifuged, washed twice with water, and dried overnight at 85 °C.

In preparing $Nd_2Sn_xZr_{2-x}$ compositions, the above preformed x(NdSn) and (2-x)NdZr (x=0.5, 1, and 1.5) precipitates were combined, suspended in water, stirred vigorously for 2 h, followed by the removal of water using a centrifuge. The resultant precipitate was dried overnight at 85 °C. These powders with nominal composition $Nd_2Sn_xZr_{2-x}$ (where x=0, 0.5, 1, 1.5, and 2) were calcined at 800 °C for 4 h. Following calcination, a portion of the powders were sintered at 1400 °C for 50 h in air. The remainder of the calcined powder was compacted into pellets using a uniaxial press at 2.0–2.5 MPa, and then sintered in air under a range of conditions (24–50 h between 1200 °C and 1550 °C).

Raman spectra were collected to investigate the structural evolution of the calcined materials using a Renishaw in Via Raman spectrometer equipped with the Argon ion laser (514 nm) and a Peltier cooled CCD detector (Renishaw plc, Old Town, Gloucestershire, UK). Stokes shifted Raman spectra were collected in the static mode in the range of 200–800 cm^{-1} with a spectral resolution of 1.7 cm^{-1} for the 1800 l/mm grating. On average 20 spectra were collected for each sample. The spot size was approximately 1.5 μm for 50 × magnification.

X-ray diffraction (XRD) patterns were also collected to confirm the crystal structure using a PANalytical X'Pert Pro diffractometer (Almelo, the Netherlands) using Cu K_α radiation (λ=1.541874 Å) at 45 kV and 40 mA. The data were recorded over an angular range of 10–80° (2θ) with a step size of 0.03° and an acquisition time of 2 s per step.

A JEOL JEM 2010F (JEOL Ltd., Akishima, Tokyo, Japan) transmission electron microscope (TEM), equipped with a field emission gun (FEG) electron source operated at 200 kV, was used to record selected area electron diffraction patterns of representative grains. The images were recorded with a CCD camera mounted in the 35 mm port above the TEM viewing chamber (Model 782, Gatan, Pleasanton, CA). Samples for TEM were prepared by suspending powder in ethanol and depositing several drops onto a carbon coated 200-mesh copper grid.

Scanning electron microscopy (SEM) was used to analyze the grain morphology and porosity of the sintered pellets. Samples were examined by Zeiss Ultra Plus scanning electron microscope (Carl Zeiss NTS GmbH, Oberkochen, Germany) with an accelerating voltage of 20 kV. Samples were mounted in an epoxy resin and polished to 1 μm diamond finish. A thin carbon film (~5 nm) was deposited onto the polished surface.

Archimedes' displacement method was used to measure ceramic bulk density and porosity using distilled water as the medium. In this case, the porosity refers to the percentage ratio of the volume of open pores to the bulk volume of the ceramic.

3. Results and discussion

Fig. 1 shows the XRD patterns for $Nd_2Sn_xZr_{2-x}O_7$ (x=0, 0.5, 1, 1.5, and 2) powders sintered at 1400 °C for 50 h. The pyrochlore superstructure reflections, *i.e.* (111), (311), (331), and (511) are clearly evident in two samples $Nd_2Zr_2O_7$ and $Nd_2Sn_{0.5}Zr_{1.5}O_7$, indicating the formation of the pyrochlore structure. The remaining samples show the (331) and (511) reflections which are most pronounced. Further observation of the XRD patterns reveal that both $Nd_2Zr_2O_7$ and

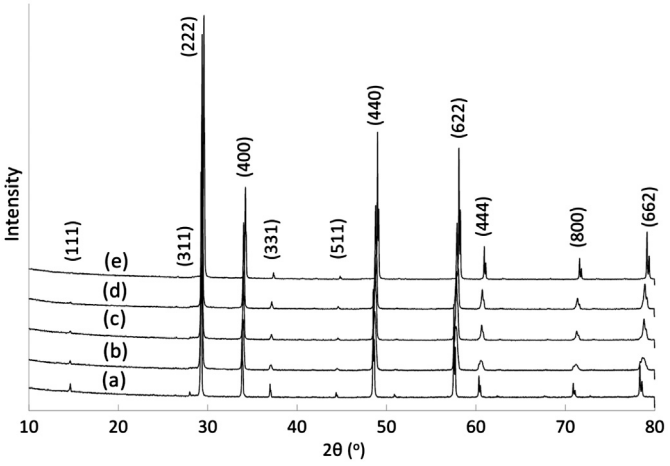

Fig. 1. XRD patterns of powder samples for (a) $Nd_2Zr_2O_7$, (b) $Nd_2Sn_{0.5}Zr_{1.5}O_7$, (c) Nd_2SnZrO_7, (d) $Nd_2Sn_{1.5}Zr_{0.5}O_7$, and (e) $Nd_2Sn_2O_7$, sintered at 1400 °C for 50 h.

Table 1
Lattice parameter (Å) of various pyrochlore materials.

Sample	This work[a]	Experimental[17]	Calculated[17]
$Nd_2Zr_2O_7$	10.6536(1)	10.676 ± 0.0344 10.68 ± 0.0384 10.648 ± 0.0064 10.666 ± 0.0244	10.6416
$Nd_2Sn_{0.5}Zr_{1.5}O_7$	10.6226(3)	n/a	
Nd_2SnZrO_7	10.5904(4)	n/a	
$Nd_2Sn_{1.5}Zr_{0.5}O_7$	10.5835(2)	n/a	
$Nd_2Sn_2O_7$	10.5731(2)	10.567+0.0440	10.5230

[a]Error on the last digit is displayed in parentheses.

$Nd_2Sn_2O_7$ samples (Fig. 1a and e) have distinct sharp diffraction peaks suggesting these two materials have a higher degree of crystallinity; whereas samples with mixed composition of Zr and Sn at the B sites display broader diffraction peaks, suggesting a systematic lattice change and variations in crystallinity. A gradual peak shift towards larger angles, especially at the high end of 2θ, suggests that the lattice unit size becomes smaller with the increasing amount of Sn atoms at the B sites. These observations are confirmed by the calculation of the pyrochlore unit cell parameters using the Le Bail fit of XRD data and the Rietica software, depicted in Table 1. In comparison to previously published unit cell data, both $Nd_2Zr_2O_7$ and $Nd_2Sn_2O_7$ pyrochlores are in a good agreement with the published data [17]. The ionic radii of Sn^{4+} and Zr^{4+} are 0.0690 and 0.0720 nm, respectively, for 6-fold coordination [18]. For samples with mixed composition of Sn and Zr, a small difference between the ionic radii of these two ions may lead to a random occupation of the B sites by each element, and their effect on crystal structure will be discussed in later section.

Analyses of X-ray data show [17] that even the consideration of ionic radii alone gave satisfactory results when applied to $A_2B_2O_7$ pyrochlores to predict the lattice constant, the results were not as predictable when considering mixed cation and anion pyrochlores. Both the ionic radii and the electronegativity differences are important in defining the lattice constants of mixed pyrochlores. One of the possible reasons for this discrepancy is the random distribution of cations and anions of different types over the crystallographic sites of the pyrochlore lattice, which produces considerable variation of the electron density in such crystals. The chemical bonding in mixed pyrochlores is complex leading to varying degrees of ionic and covalent character of the metal-ligand bonding that is driven by the electronegativity of the constituting cations and anions of the pyrochlore composition. This gives rise to XRD peaks in pyrochlores with mixed B sites that are not as well indexed as those having a single component on the B site.

While XRD is more sensitive to disorder in the cation sub-lattice than the anion sub-lattice (since the X-ray scattering power of oxygen is much less than metal cations), Raman spectroscopy is very sensitive to metal–oxygen vibrational modes. In the Raman spectra the A and B cations do not contribute to the vibrations since they are located on the inversion center and only vibrations of the oxygen atoms are allowed. As a result, Raman spectroscopy has been extensively used to study the crystalline-to-amorphous transitions and the extent of disorder in the pyrochlore structures [19–22].

The basic cell of $A_2B_2O_7$ cubic pyrochlore is often presented as an assembly of BO_6 octahedra linked by A_2O' chains. Vandenborre et al. [19] described this structure as being made up of two different types of chemical bonds where the B–O bonds are more rigid, relatively covalent and ensure the cohesion of the structure $A_2B_2O_7$. These bonds are sensitive to very small changes in either chemical or structural environment. The A–O bonds are much weaker and thought to be of ionic character. A factor group analysis predicts six Raman active modes ($A_{1g}+E_g+4F_{2g}$) for the ideal pyrochlore structure [19–22]. The A_{1g}, E_g and three out of four F_{2g} modes are usually assigned to the vibration of the BO_6 octahedra, while the forth F_{2g} mode is typically found at the lower frequency range and is thought to be due to the O–A–O′ vibrations [19–25]. The atomic motions associated with the A_{1g} and E_g modes involve only the displacements of the oxygen atoms on the 48f site relative to other atoms in the unit cell, while the Raman-active F_{2g} modes involve the displacements of oxygen atoms on both the 48f and 8a sites.

In the literature the assignment of Raman bands varies significantly for different pyrochlore materials [19–25]. Nevertheless, the Raman spectra for the pyrochlore structure is produced entirely by the vibrations of the anion substructure, only minor differences in the Raman frequencies are expected between zirconate and stannate pyrochlores due to the differences in the nature of A and B cations. Therefore in this study, the assignment of Raman active modes was undertaken by comparison to other pyrochlore structured materials [26,27] and first-principle calculations found in the literature [25,28].

Fig. 2 shows Raman spectra of various composition $Nd_2Sn_xZr_{2-x}O_7$ ($x=0$–2) sintered at 1400 °C for 50 h and the peaks position is provided in Table 2. Three broad Raman bands are observed in the spectrum $Nd_2Zr_2O_7$, they have been assigned to the A_{1g} mode at ~508 cm^{-1}, E_g at ~301 cm^{-1} and F_{2g} mode at ~400 cm^{-1} (Fig. 2a). The line broadening in zirconate pyrochlores indicates a certain degree of disorder, believed to be due to the atomic displacement from ideal positions [20,21,26]. Even though XRD patterns show the pyrochlore superstructure reflections for these compounds, when the Zr^{4+} ions are substituted at the B site of the lattice with the Sn^{4+} ions, additional F_{2g} modes around 336 and 527 cm^{-1} become apparent (Fig. 2d and e). The vibrational spectrum of stannate pyrochlore ($Nd_2Sn_2O_7$) (Fig. 2e) shows

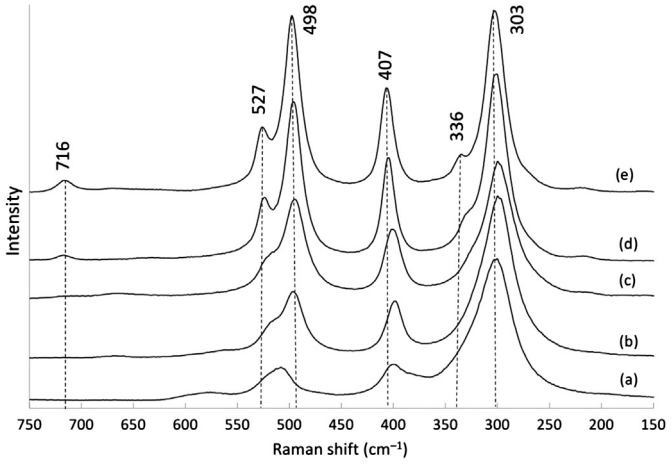

Fig. 2. Raman spectra of powder samples for (a) $Nd_2Zr_2O_7$, (b) $Nd_2Sn_{0.5}Zr_{1.5}O_7$, (c) Nd_2SnZrO_7, (d) $Nd_2Sn_{1.5}Zr_{0.5}O_7$, and (e) $Nd_2Sn_2O_7$, sintered at 1400 °C for 50 h.

Table 2
Raman peaks (cm^{-1}) of various pyrochlore materials.

Mode	$Nd_2Sn_2O_7$	$Nd_2Sn_{1.5}Zr_{0.5}O_7$	Nd_2SnZrO_7	$Nd_2Sn_{0.5}Zr_{1.5}O_7$	$Nd_2Zr_2O_7$
F_{2g}	527	524	520, *sh*	516, *sh*	–
A_{1g}	498	496	495	496	508
F_2t_g	407	405	401	399	400
F_{2g}	336	330, *sh*	–	–	–
E_g	303	302	299	300	301

sh refers to shoulder peak.

frequencies are well-resolved and the structure is very close to the ideal pyrochlore. Thus, the substitution of Zr at the B sites by a smaller ionic radius ion (Sn) resulted in more ordered pyrochlore material as evident by the Raman data. This is possibly due to the differences in the ionic radius ratios (r_A^{3+}/r_B^{4+}) which according to Subramanian [29] govern the formation and stability of the oxide pyrochlores. Under ambient conditions, the cation ionic radius ratio (r_A/r_B) for the stable III/IV phase pyrochlore lies between 1.46 and 1.78 [29]. The $Nd_2Sn_2O_7$ pyrochlore has a cation radius ratio of 1.63 in comparison to 1.56 for the $Nd_2Zr_2O_7$ and therefore is very close to the ideal pyrochlore structure and so, is especially stable.

Furthermore, the wavenumbers of all Raman active modes are practically constant (Table 2, Fig. 2), with variance of less than 2% calculated for all modes, despite the substitution of atoms at the B sites (while the A atom remains the same). Since the mass of Sn atom is greater than the Zr atom, the force constant also increased resulting in a stronger and therefore shorter Sn–O bond in comparison with the Zr–O bond. Therefore this observation is in perfect agreement with the XRD data which indicate the lattice unit cell parameters decrease gradually with the increasing amount of Sn atoms at the B sites (Table 1).

There are two additional features evident in the spectrum of $Nd_2Sn_2O_7$ (Fig. 2e). A broad shoulder on the low wavenumber side of the E_g peak, which possibly corresponds to the F_{2g} Raman active mode [25,30], and a small peak found at 716 cm^{-1}. This peak is often assigned to the distortion of the octahedral BO_6 [19] or a combination and/or overtone band [25]. It is worth noting here however that *ab initio* calculations by Fischer [28] predict an F_{2g} mode to have a frequency as high as 880 cm^{-1}. Therefore the exact location of the F_{2g} fourth mode remains questionable.

Selected area electron diffraction (SAED) patterns were recorded for the samples sintered at 1400 °C for 50 h, which are displayed in Fig. 3. These SAED patterns were taken in the [110] zone axis orientation from a single large grain for each sample and they exhibit a classical pyrochlore pattern with sharp super-lattice intensities interposed with relatively stronger fluorite sub-cell intensities. These results are in good agreement with the XRD and Raman data.

Fig. 4 shows backscattered SEM images of the polished surfaces for pellet samples of $Nd_2Sn_xZr_{2-x}O_7$ ($x=0$–2) sintered at 1550 °C for 24 h. Bulk density and apparent porosity values calculated for different sintering conditions are given in Table 3. As expected, increasing the sintering temperature led to higher density in all compositions. The apparent porosity of $Nd_2Zr_2O_7$ and $Nd_2Sn_2O_7$ sintered at 1200 °C was approximately 14% and 62%, respectively. Increasing the sintering temperature from 1200 °C to 1550 °C reduced the apparent porosity of the $Nd_2Zr_2O_7$ ceramic to 8%, however only a small decrease (in terms of the changing percentage) was recorded for $Nd_2Sn_2O_7$, which exhibited a 51% apparent porosity. One possible reason for this result is that both Nd and Sn elements were precipitated separately during the synthetic procedure, thereby creating a segregated oxide nanostructure at low calcination temperatures [31]. This presumably would lead to the formation of discrete Nd_2O_3 and SnO_2 oxides during the heat treatment process. Support for this pathway can be found in the Raman spectra for the NdSn-based powders calcined at 800 °C and 1000 °C. Both materials show a strong band at 325 cm^{-1} and a broad peak centered around 640–630 cm^{-1} which are the major Raman modes in Nd_2O_3 and SnO_2 oxides, respectively (data not shown here). These modes are not observed in the $Nd_2Sn_2O_7$ pyrochlore material sintered at 1400 °C and above.

It is well known that pure SnO_2 is difficult to densify via traditional sintering protocols because of the predominance of non-densifying mechanisms for mass transport, such as surface diffusion and evaporation-condensation [5]. This might explain why the apparent porosity of the $Nd_2Sn_2O_7$ pyrochlore material was higher than that of $Nd_2Zr_2O_7$ material. Compared with sub-micron to micron sized particles used in solid state reactions, discrete Nd_2O_3 and SnO_2 with nanostructure morphologies were expected to improve sintering [2], however, this improvement is limited due to the intrinsic physicochemical properties of pure SnO_2. One strategy that could improve the densification of Sn−containing pyrochlores is to inhibit the formation of SnO_2 phase during the calcination step. This may be possible by chemical modification of the original precursors to form a complex precipitate such as Nd–R–Sn (R = organic ligand) that would assist in phase assemblage.

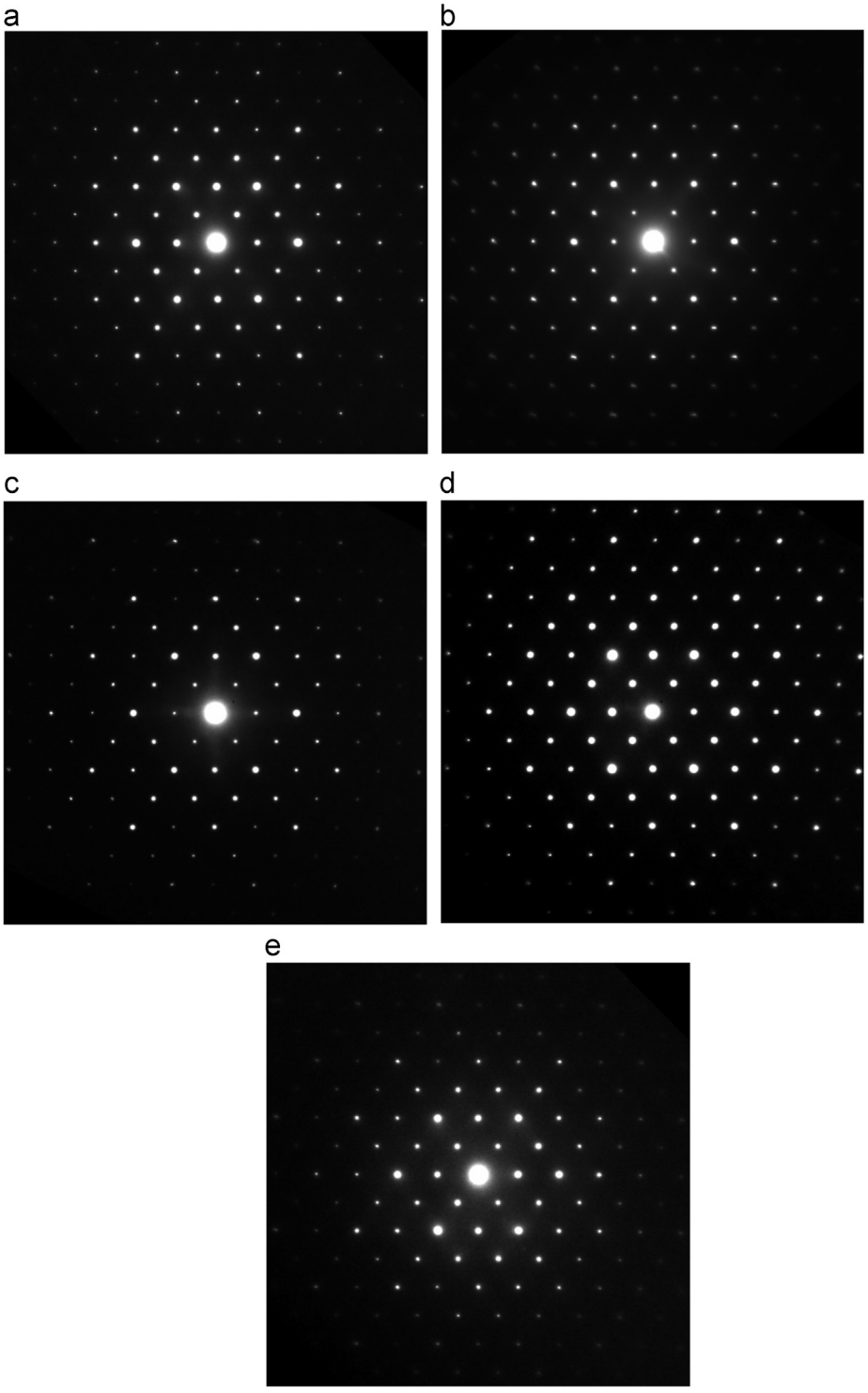

Fig. 3. Selected area diffraction patterns of powder samples for (a) $Nd_2Zr_2O_7$, (b) $Nd_2Sn_{0.5}Zr_{1.5}O_7$, (c) Nd_2SnZrO_7, (d) $Nd_2Sn_{1.5}Zr_{0.5}O_7$, and (e) $Nd_2Sn_2O_7$, sintered at 1400 °C for 50 h. All patterns were taken down the [110] zone axis.

Better compaction of the green powder pellet would also assist in eliminating porosity during sintering.

Given that dense $Nd_2Zr_2O_7$ pyrochore ceramics have been prepared by our novel synthesis procedure, the substitution of small dopant quantities of Sn into $Nd_2Zr_2O_7$ pyrochore should not impact greatly on the sintering and therefore the final bulk density of the ceramic. Finally, achieving high density ceramics with compositions centered on pure zirconate or zirconate containing small amount of stannates could provide a robust matrix for radiation tolerance and therefore further investigations are underway to qualify ion irradiation effects on these ceramics.

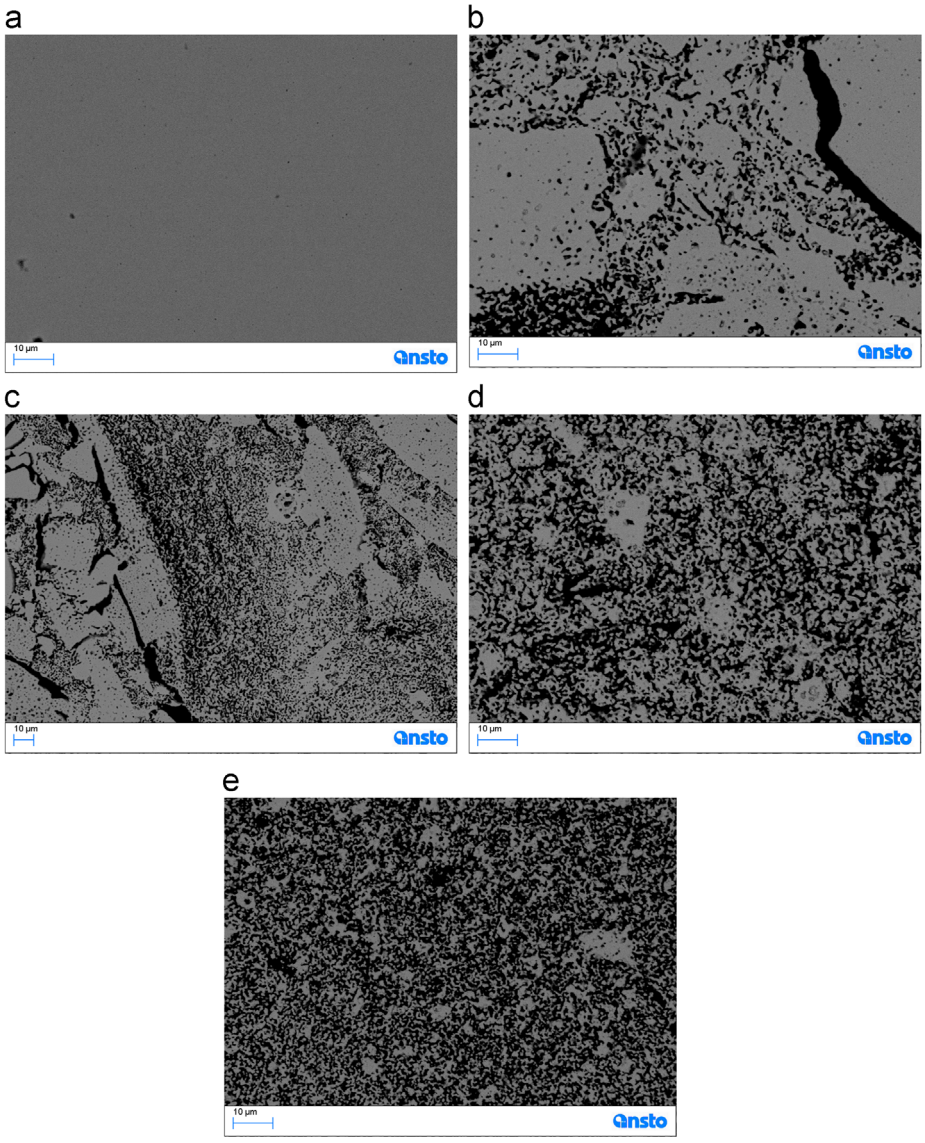

Fig. 4. Backscattered scanning electron micrographs of the polished surfaces of pelletized samples (a) $Nd_2Zr_2O_7$, (b) $Nd_2Sn_{0.5}Zr_{1.5}O_7$, (c) Nd_2SnZrO_7, (d) $Nd_2Sn_{1.5}Zr_{0.5}O_7$, and (e) $Nd_2Sn_2O_7$, sintered at 1550 °C for 24 h. The black regions are pores.

Table 3
Bulk density (g/cm^3) and apparent porosity of $Nd_2Sn_xZr_{2-x}O_7$ compositions sintered over a range of temperature/time conditions.

Sample	1200 °C/50 h	1400 °C/50 h	1550 °C/24 h
$Nd_2Zr_2O_7$	5.38/14.0%	5.86/12.1%	5.90/8.0%
$Nd_2Sn_{0.5}Zr_{1.5}O_7$	3.54/43.1%	4.40/28.5%	4.88/24.4%
Nd_2SnZrO_7	3.06/52.8%	3.83/42.3%	4.53/31.3%
$Nd_2Sn_{1.5}Zr_{0.5}O_7$	2.86/57.2%	3.23/53.2%	3.66/46.8%
$Nd_2Sn_2O_7$	2.68/61.8%	3.21/54.8%	3.51/51.0%

4. Conclusions

Neodymium stannate zirconate $Nd_2Sn_xZr_{2-x}O_7$ ($x=0$–2) with pyrochlore superstructure have been produced by the complex-precipitation method. The chemical reaction takes place at the molecular level ensuring the formation of reactive powders. Raman and X-ray diffraction analysis confirmed the formation of the pyrochlore structure. Pure phase $Nd_2Zr_2O_7$ pyrochlore ceramic was prepared yielding high bulk density, however, Sn substituted into the pyrochlore structure with compositions $>25\%$ Sn were challenging and difficult to sinter to closed porosity, even at temperature as high as 1550 °C. Finally, unlike conventional mixed oxide methods or traditional sol–gel processing of refractory oxide ceramics, the synthesis protocol described in this study was undertaken in an aqueous phase, eliminating the use for organic solvents and/or mechanical milling steps in powder preparation.

References

[1] J.-F. Hochepied, M.-H. Berger, F. Dynys, A. Dessombz, A. Sayir, Aqueous co-precipitated $Ti_{0.5}Sn_{0.5}O_2$ nanopowders as precursors for dense spinodally

decomposed ceramics, Journal of the American Ceramics Society 94 (2011) 4226–4230.
[2] I. Safaee, M.A. Bahrevar, M.M. Shahraki, S. Baghshahi, K. Ahmadi, Microstructural characteristics and grain growth kinetics of Pr_6O_{11} doped SnO_2-based varistors, Solid State Ionics 189 (2011) 13–18.
[3] W. Hamd, Y.C. Wu, A. Boulle, E. Thune, R. Guinebretière, Microstructural study of SnO_2 thin layers deposited on sapphire by sol–gel dip-coating, Thin Solid Films 518 (2009) 1–5.
[4] A. Maître, D. Beyssen, R. Podor, Modelling of the grain growth and the densification of SnO_2-based ceramics, Ceramics International 34 (2008) 27–35.
[5] A. Maître, D. Beyssen, R. Podor, Effect of ZrO_2 additions on sintering of SnO_2-based ceramics, Journal of European Ceramics Society 24 (2004) 3111–3118.
[6] P.R. Bueno, E.R. Leite, L.O.S. Bulhões, E. Longo, C.O. Paiva-Santos, Sintering and mass transport features of $(Sn,Ti)O_2$ polycrystalline ceramics, Journal of European Ceramics Society 23 (2003) 887–896.
[7] J. Lian, K.B. Helean, B.J. Kennedy, L.M. Wang, A. Navrotsky, R.C. Ewing, Effect of structure and thermodynamic stability on the response of lanthanide stannate pyrochlores to ion beam irradiation, Journal of Physical Chemistry B 110 (2006) 2343–2350.
[8] M. Lang, F. Zhang, J. Zhang, J. Wang, J. Lian, W.J. Weber, B. Schuster, C. Trautmann, R. Neumann, R.C. Ewing, Review of $A_2B_2O_7$ pyrochlore response to irradiation and pressure, Nuclear Instruments and Methods in Physics Research Section B 268 (2010) 2951–2959.
[9] A.E. Ismail, J.A. Greathouse, P.S. Crozier, S.M. Foiles, Electron-ion coupling effects on simulations of radiation damage in pyrochlore waste forms, Journal of Physics: Condensed Matter 22 (2010) 225405.
[10] R.C. Ewing, W.J. Weber, J. Lian, Nuclear waste disposal—pyrochlore ($A_2B_2O_7$): nuclear waste form for the immobilization of plutonium and minor actinides, Journal of Applied Physics 95 (2004) 5949–5971.
[11] S. Lutique, D. Staicu, R.J.M. Konings, V.V. Rondinella, J. Somers, T. Wiss, Zirconate pyrochlore as a transmutation target: thermal behaviour and radiation resistance against fission fragment impact, Journal of Nuclear Materials 319 (2003) 59–64.
[12] R.C. Ewing, W.J. Weber, F.W. Clinard Jr., Radiation effects in nuclear waste forms for high-level radioactive waste, Progress in Nuclear Energy 29 (1995) 63–127.
[13] L. Minervini, R.W. Grimes, Disorder in pyrochlore oxides, Journal of the American Ceramic Society 83 (2000) 1873–1878.
[14] G.R. Lumpkin, M. Pruneda, S. Rios, K.L. Smith, K. Trachenko, K.R. Whittle, N.J. Zaluzec, Nature of the chemical bond and prediction of radiation tolerance in pyrochlore and defect fluorite compounds, Journal of Solid State Chemistry 180 (2007) 1512–1518.
[15] G.R. Lumpkin, K.L. Smith, M.G. Blackford, K.R. Whittle, E.J. Harvey, S.A.T. Redfern, N.J. Zaluzec, Ion irradiation of ternary pyrochlore oxides, Chemistry of Materials 21 (2009) 2746–2754.
[16] M. de los Reyes, K.R. Whittle, Z. Zhang, S.E. Ashbrook, M.R. Mitchell, L.-Y. Jang, G.R. Lumpkin, The pyrochlore to defect fluorite phase transition in $Y_2Sn_{2-x}Zr_xO_7$, Royal Socity of Chemistry Advances 3 (2013) 5090–5099.
[17] M.G. Brik, A.M. Srivastava, Pyrochlore structural chemistry: predicting the lattice constant by the ionic radii and electronegativities of the constituting ions, Journal of the American Ceramic Society 95 (2012) 1454–1460.
[18] R.D. Shannon, Revised effective ionic radii and systematic studies of interatomic distances in halides and chalcogenides, Acta Crystallographica A32 (1976) 751–767.
[19] M.T. Vandenborre, E. Husson, J.P. Chatry, D. Michel, Rare-earth titanates and stannates of pyrochlore structure; vibrational spectra and force fields, Journal of Raman Spectroscopy 14 (1983) 63–71.
[20] D. Michel, M.P.Y. Jorba, R. Collongues, Study by Raman spectroscopy of order-disorder phenomena occurring in some binary oxides with fluorite-related structures, Journal of Raman Spectroscopy 5 (1976) 163–180.
[21] B.E. Scheetz, W.B. White, Characterization of anion disorder in zirconate $A_2B_2O_7$ compounds by Raman spectroscopy, Journal of the American Ceramic Society 62 (1979) 468–470.
[22] M.T. Vandenborre, E. Husson, Comparison of the force field in various pyrochlore families. I. The $A_2B_2O_7$ oxides, Journal of Solid State Chemistry 50 (1983) 362–371.
[23] T.T. Zhang, K.W. Li, J. Zeng, Y.L. Wang, X.M. Song, H. Wang, Synthesis and structural characterization of a series of lanthanide stannate pyrochlores, Journal of Physics and Chemistry of Solids 69 (2008) 2845–2851.
[24] F. Rosi, V. Manuali, C. Miliani, B.G. Brunetti, A. Sgamellotti, T. Grygar, D. Hradil, Raman scattering features of lead pyroantimonate compounds. Part I: XRD and Raman characterization of $Pb_2Sb_2O_7$ doped with tin and zinc, Journal of Raman Spectroscopy 40 (2009) 107–111.
[25] D.J. Arenas, L.V. Gasparov, W. Qiu, J.C. Nino, C.H. Patterson, D.B. Tanner, Raman study of phonon modes in bismuth pyrochlores, Physical Review B 82 (2010) 214302.
[26] N.J. Hess, B.D. Begg, S.D. Conradson, D.E. McCready, P.L. Gassman, W.J. Weber, Spectroscopic investigations of the structural phase transition in $Gd_2(Ti_{1-y}Zr_y)_2O_7$ pyrochlores, Journal of Physical Chemistry B 106 (2002) 4663–4677.
[27] B.P. Mandal, M. Pandey, A.K. Tyagi, $Gd_2Zr_2O_7$ pyrochlore: potential host matrix for some constituents of thoria-based reactor's waste, Journal of Nuclear Materials 406 (2010) 238–243.
[28] M. Fischer, T. Malcherek, U. Bismayer, P. Blaha, K. Schwarz, Structure and stability of $Cd_2Nb_2O_7$ and $Cd_2Ta_2O_7$ explored by *ab initio* calculations, Physical Review B 78 (2008) 014108.
[29] M.A. Subramanian, G. Aravamudan, G.V. Subba Rao, Oxide pyrochlores—A review, Progress in Solid State Chemistry 15 (1983) 55–143.
[30] G. Sattonnay, S. Moll, L. Thomé, C. Decorse, C. Legros, P. Simon, J. Jagielski, I. Jozwik, I. Monnet, Phase transformations induced by high electronic excitation in ion-irradiated $Gd_2(Zr_xTi_{1-x})_2O_7$ pyrochlores, Journal of Applied Physics 108 (2010) 103512.
[31] L. Kong, I. Karatchevtseva, M.G. Blackford, N. Scales, G. Triani, Aqueous chemical synthesis of $Ln_2Sn_2O_7$ pyrochlore structured ceramics, Journal of the American Ceramic Society (2013) http://dx.doi.org/10.1111/jace.12409, in press.